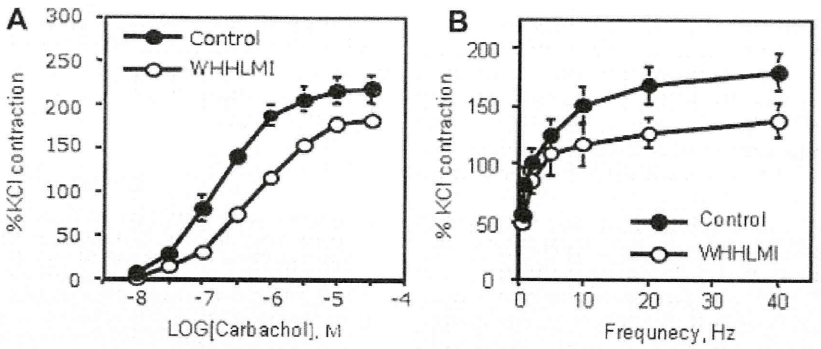

Fig. 2. Concentration–response curves to carbachol (**A**) and frequency–response curves to EFS (**B**) in the isolated detrusor smooth muscles of WHHLMI rabbits (○) **and the control rabbits (●). The contractile responses were showed as % of 80 mM KCl-induced contractions. Each point represents the mean ± SEM, if not shown, SEM bars fall within the size of the symbols.**

induced poor blood supply to bladder may be related to bladder dysfunction. It is interesting that the WHHLMI rabbits showed almost same results as rabbits with severe bladder ischemia reported by Azadzoi et al.[6] On the other hand, Shenfeld et al.[16] reported that gradual onset of atherosclerosis in apolipoprotein E gene knockout mice did not caused significant changes in bladder smooth muscle contractile responses to bethanechol, KCl, or resting tone. Although differences in the experimental animal and severity of atherosclerosis may contribute to the different results between the report and the present study, further studies will be required to clarify the reasons.

WHHLMI rabbits showed a significant increase in CGRP positive neurons. CGRP is one of the predominant excitatory neurotransmitters in mediating sensory perception, and an important nociceptive marker.[17] CGRP has a major role in mediating hypersensitivity in many systems, including lower urinary tract.[18] The increased CGRP positive neurons in WHHLMI rabbits might cause the enhanced afferent activity, resulting in urinary frequency and detrusor overactivity. Nerve growth factor (NGF) seems to control, at least partly, survival and outgrowth of CGRP positive neurons through its tyrosine kinase receptor A. It has been reported that the increases in NGF and CGRP positive neurons have strong relationship with detrusor overactivity in spinal cord injured rats.[19] The same mechanism may contribute to the detrusor overactivity observed in WHHLMI rabbits. It is suggested that NGF distribution is related to the increase in CGRP positive neurons. Further evaluation will be needed in this point. On the contrary, WHHLMI rabbits showed a significant decrease of S-100 protein positive neurons (denervation), which may contribute to the decreased contractility of bladder smooth

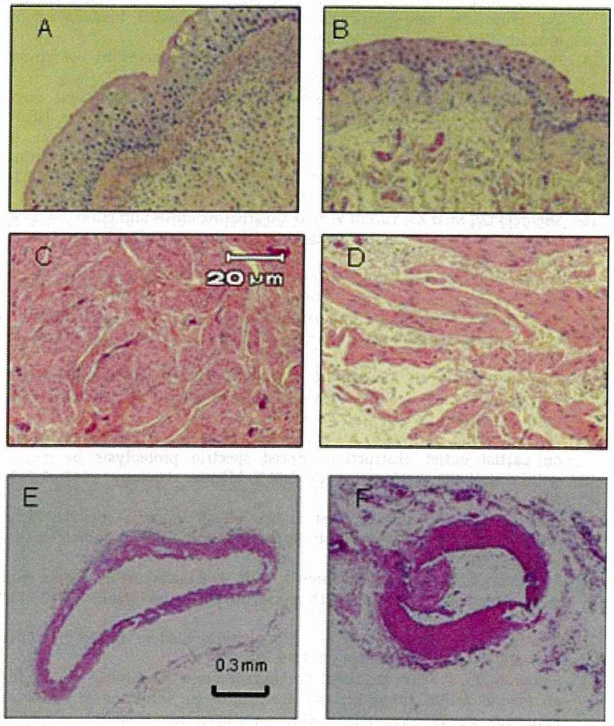

Fig. 3. Histological findings of the bladder and distal portion of internal iliac artery in the control (**A**,**C**,**E**) and WHHLMI (**B**,**D**,**F**) rabbits. The urothelium of WHHLMI rabbits (B) was thinner than that of the control (A), and smooth muscle area of WHHLMI rabbits (D) decreased with replacement by connective tissues. In WHHLMI rabbits, atherosclerosis lesions and thickening of media (F) were observed, as compared to the control (E).

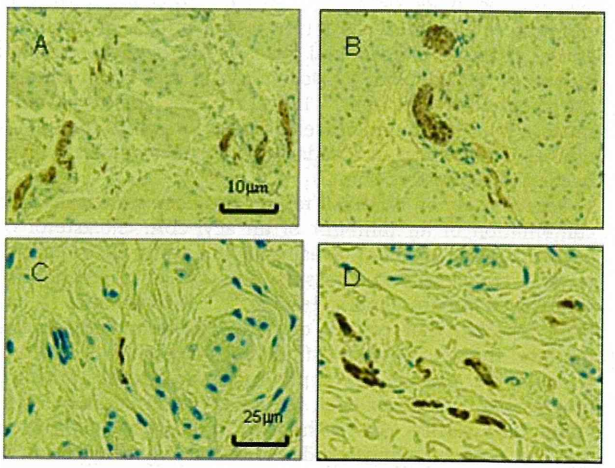

Fig. 4. Immunohistochemical stainings for S-100 positive neurons (**A**: control rabbits and **B**: WHHLMI rabbits) and CGRP positive neurons (**C**: control rabbits and **D**: WHHLMI rabbits). S-100 positive neurons were mainly found in smooth muscle layer, and CGRP-positive neurons mainly found under epithelium. Bladder of the WHHLMI rabbits showed smaller number of S-100 positive neurons (B) and greater number of CGRP positive neurons (D), as compared to the control rabbits (A,C).

muscles to stimulations. Although the mechanism of denervation is not fully understood, Ca^{2+}-dependent neutral protease calpain may be activated by ischemia and result in the proteolysis of neuronal membranes.[20] Histological study of bladder in WHHLMI rabbits showed the fibrosis of bladder wall and the decreased amount of detrusor smooth muscles, which may also contribute to the decreased bladder contractility.

The bladder dysfunction observed in WHHLMI rabbits might be described as the state of detrusor hyperactivity with impaired contraction which can be clinically experienced in human elderly. Although we did not evaluate the time-dependent changes in bladder function in WHHLMI rabbits, bladder dysfunction observed in this study might be a decompensate state after peripheral nervous system activated and reorganized to compensate hyperlipidemia and chronic ischemia with structural an functional changes of bladder. Azadzoi et al. suggested that severe bladder ischemia caused much severe fibrosis, which may be related to a significant increase in the expression of transforming growth factor beta-1 (TGF-β1), and that fibrosis might play a major role in bladder dysfunction.[5] They also speculated that detrusor overactivity observed in rabbits with moderate bladder ischemia was partly because of increased interstitial K^+ concentration in the detrusor, which was derived by decreased K^+ washout due to reduced blood flow.[6] They also suggested that lipoxygenase and cyclooxygenase pathways may affect bladder condition and that leukotrienes may overcome the effect of prostaglandin pathway under ischemic state, resulting in detrusor overactivity.[7]

The unique point in the present study is that bladder weight did not increase and bladder urothelium became thinner; whereas in other experimental models such as BOO, spinal cord injured, and bladder ischemia, bladder weight increased and urothelium appeared thickened, edematous and hyperemic.[5–7,20–22] In addition to the difference in urothelium compensation processes in the various experimental conditions, the presence and degree of inflammation or metabolic changes related to hyperlipidemia may account for urothelium thinning observed in the WHHLMI rabbits, although serum hyperlipidemia alone seems not to cause epithelium thinning.[5,23] Another possibility is the effects of oxidative stress. Reactive oxygen and reactive nitrogen species are known to be generated by ischemia, and they could damage the membrane function.[21] Those changes might promote mucosa thinning and increased permeability of urothelium as well as denervation in bladder wall. Further studies will be needed to clarify this point.

Recent study on WHHLMI rabbits has been shown that the combination of an inhibitor of an acyl-CoA: cholesterol *O*-acyltransferase inhibitor (avasimibe) to a statin (atrovastatin) is able to prevent progression and induce regression of established atherosclerotic lesions.[24,25] Furthermore, it has been reported that control of hyperlipidemia with statins inhibits the progression of kidney disease.[26] Therefore, it might be possible to apply those medicines to retard progression of LUTS or even reduce them. In addition, such study may clarify the mechanism of bladder dysfunction induced by chronic hyperlipidemia and slowly progression of atherosclerosis with bladder ischemia.

CONCLUSIONS

This study demonstrated that WHHLMI rabbits showed detrusor overactivity with decreased detrusor contractility. It is suggested that chronic hyperlipidemia contributes to bladder dysfunction and pathophysiology of LUTS. Furthermore, WHHLMI rabbits may be a useful model for evaluation of pathophysiology of LUTS and exploration of future treatment possibilities.

REFERENCES

1. Homma Y, Yamaguchi O, Hayashi K, The Members of the Neurogenic Bladder Society Committee. An epidemiological survey of overactive bladder symptoms in Japan. BJU Int 2005;96:1314–8.
2. Reeves P, Irwin D, Kelleher C, et al. The current and future burden and cost of overactive bladder in five European countries. Eur Urol 2006;50:1050–7.
3. Rahman NU, Phonsombat S, Bochinski D, et al. An animal model to study lower urinary tract symptoms and erectile dysfunction: The hyperlipidaemic rat. BJU Int 2007;100:658–63.
4. Lee WC, Chien CT, Yu HJ, et al. Bladder dysfunction in rats with metabolic syndrome induced by long-term fructose feeding. J Urol 2008;179:2470–6.
5. Azadoi KM, Tarcan T, Siroky M, et al. Atherosclerosis-induced chronic ischemia causes bladder fibrosis and non-compliance in the rabbit. J Urol 1996;161:1626–35.
6. Azadzoi KM, Tarcan T, Kozlowski R, et al. Overactivity and structural changes in the chronically ischemic bladder. J Urol 1999;162:1768–78.
7. Azadzoi KM, Shinde VM, Tarcan T, et al. Increased leukotriene and prostaglandin release, and overactivity in the chronically ischemic bladder. J Urol 2003;169:1885–91.
8. Watanabe T. Serial inbreeding of rabbits with hereditary hyperlipidemia (WHHL-rabbit). Atherosclerosis 1980;36:261–8.
9. Shiomi M, Ito T, Yamada S, et al. Development of an animal model for spontaneous myocardial infarction (WHHLMI rabbit). Arterioscler Thromb Vasc Biol 2003;23:1239–44.
10. Shiomi M, Fun J. Unstable coronary plaques and cardiac events in myocardial infarction-prone Watanabe heritable hyperlipidemic rabbits: Questions and quandaries. Curr Opin Lipidol 2008;19:631–6.
11. Ito T, Shiomi M. Cerebral atherosclerosis occurs spontaneously in homozygous WHHL rabbits. Atherosclerosis 2001;156:57–66.
12. Yoshida M, Homma Y, Inadome A, et al. Age-related changes in cholinergic and purinergic neurotransmission in human isolated bladder smooth muscles. Exp Gerontol 2001;36:99–109.
13. Ferrandino I, Grimaldi MC. S-100-immunoreactive nerves in the urinary bladder of the rat. Eur J Histochem 1995;39:127–32.
14. Collins JJ, Wilson K, Fischer-Colbrie R, et al. Distribution and origin of secretoneurin-immunoreactive nerves in the female rat uretus. Neuroscience 2000;95:255–64.
15. Van Poppel H, Stessens R, Baert L, et al. Endoscopic biopsies for quantitative nerve density evaluation of the urinary bladder. Eur Urol 1988;14:236–9.
16. Shenfeld OZ, Meir KS, Yutkin V, et al. Do atherosclerosis and chronic bladder ischemia really play a role in detrusor dysfunction of old age? Urology 2005;65:181–4.
17. Robinson DR, Gebhart GF. Inside information—The unique features of visceral sensation. Mol Interv 2008;8:242–53.
18. Vizzard MA. Alterations in neuropeptide expression in lumbosacral bladder pathways following chronic cystitis. J Chem Neuroanat 2001;21:125–38.
19. Zinck ND, Rafuse VF, Downie JW. Sprouting of CGRP primary afferents in lumbosacral spinal cord precedes emergence of bladder activity after spinal injury. Exp Neurol 2007;204:777–90.
20. Zhao Y, Levin SS, Wein AJ, et al. Correlation of ischemia/reperfusion on partial outlet obstruction-induced spectrin proteolysis by calpain with contractile dysfunction in rabbit bladder. Urology 1997;49:293–300.
21. Juan YS, Lin WY, Kalorin C, et al. The effect of partial bladder outlet obstruction on carbonyl and nitrotyrosine distribution in rabbit bladder. Urology 2007;70:1249–53.
22. Masunaga K, Yoshida M, Inadome A, et al. Prostaglandin E_2 release from isolated bladder strips in rats with spinal cord injury. Int J Urol 2006;13:271–6.
23. Son H, Lee SL, Park WH, et al. New unstable bladder model in hypercholesterolemia rats. Urology 2007;69:186–90.
24. Shiomi M, Ito T, Tsukada T, et al. Combination treatment with troglitazone, an insulin action enhancer, and pravastatin, an inhibitor of HMG-CoA reductase, shows a synergistic effect on atherosclerosis of WHHL rabbits. Atherosclerosis 1999;142:345–53.
25. Worthley SG, Helft G, Corti R, et al. Statin therapy alone and in combination with an acyl-CoA:cholesterol *O*-acyltransferase inhibitor on experimental atherosclerosis. Pathophysiol Haemost Thromb 2007;36:9–17.
26. Fried LF. Effects of HMG-CoA reductase inhibitors (statins) on progression of kidney disease. Kidney Int 2008;100:658–63.

Jpn J Radiol (2010) 28:656–662
DOI 10.1007/s11604-010-0487-0

ORIGINAL ARTICLE

Utility of contrast-enhanced ultrasonography for qualitative imaging of atherosclerosis in Watanabe heritable hyperlipidemic rabbits: initial experimental study

Ayumi Nitta-Seko · Norihisa Nitta · Masashi Shiomi Akinaga Sonoda · Shinichi Ota · Keiko Tsuchiya Masashi Takahashi · Mineko Fujimiya · Kiyoshi Murata

Received: January 15, 2010 / Accepted: July 7, 2010

Abstract
Purpose. Using Watanabe heritable hyperlipidemic (WHHL) rabbits, we investigated the ability of ultrasonography (US) to detect contrast enhancement of atherosclerotic lesions after intravenous injection of a microbubble contrast agent (MB) and confirmed the localization of MB in the lesion by transmission electron microscopy (TEM).
Materials and methods. The abdominal aortic wall of six WHHL rabbits was observed for 20 min after MB delivery. To evaluate contrast enhancement, a region of interest (ROI) was set in the intima–media complex (IMC) and the aortic lumen. The average image brightness of the ROI was recorded as the echogenicity at each time point. Differences at each time point were analyzed by analysis of variance and the *t*-test. Histological analysis was performed after US observation.
Results. The echogenicity of the IMC was 8.48 ± 3.01 before and 10.96 ± 7.88, 32.42 ± 12.79, 24.55 ± 8.01, 17.73 ± 9.18, and 31.18 ± 13.35, respectively, at 0.5, 2, 5, 10, and 20 min after MB injection. The echogenicity of the vessel lumen was 1.16 ± 1.57, 64.21 ± 11.52, 53.59 ± 9.81, 13.32 ± 9.78, 2.63 ± 1.45, and 3.66 ± 3.01 at the corresponding time points. At 20 min after injection, the echogenicity of the IMC was significantly higher than before or 0.5 min after injection. The distribution of MB inside macrophages in atherosclerotic plaques could not be confirmed by TEM.
Conclusion. Ultrasonography was able to detect contrast enhancement of the IMC at 10 and 20 min after injection of MB.

Key words Ultrasonography contrast agent · Sonazoid · Macrophage · Vasa vasorum · Atherosclerosis

A. Nitta-Seko (✉) · N. Nitta · A. Sonoda · S. Ota · K. Tsuchiya · M. Takahashi · K. Murata
Department of Radiology, Shiga University of Medical Science, Tsukinowa-cho, Seta, Otsu 520-2192, Japan
Tel. +81-77-548-2288; Fax +81-77-544-0986
e-mail: sekoayumi@yahoo.co.jp

M. Shiomi
Institute for Experimental Animals, Kobe University School of Medicine, Kobe, Japan

M. Fujimiya
Department of Anatomy 2, Sapporo Medical University, Sapporo, Japan

Introduction

As it is difficult to identify most lesions responsible for acute coronary syndrome (ACS) or stroke by their morphological features (e.g., size, degree of vascular stenosis), the focus of previous studies was their instability.[1,2] Therefore, reliable morphological and qualitative evaluation methods are needed prior to the occurrence of events.

The intravenous (IV) ultrasonography (US) microbubble contrast agent (MB) Sonazoid is available for clinical use. As the MB enters Kupffer cells via phagocytosis, the signal intensity of the normal hepatic parenchyma increases; and lesions such as hepatocellular carcinoma (HCC) and metastatic liver tumors can be visualized by relative signal-intensity differences.[3,4]

Unlike stable plaques, most unstable plaques are rich in macrophages and are considered a high risk for ACS.[5] We posited that if MB could be directed into the atherosclerotic lesion to be phagocytosed by resident macrophages this technique would constitute a highly useful

tool for the qualitative diagnosis of atherosclerotic lesions.

We used Watanabe heritable hyperlipidemic (WHHL) rabbits to determine whether US can detect contrast enhancement of atherosclerotic lesions after IV injection of MB and checked the localization of the MB in the lesions by transmission electron microscopy (TEM).

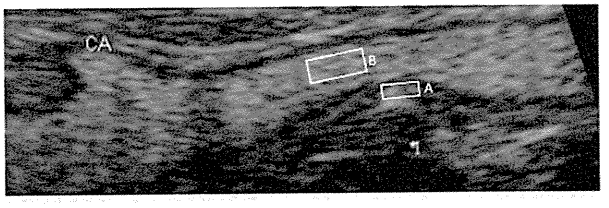

Fig. 1. Region of interest (ROI) settings in the rabbit vascular wall (*A*) and lumen (*B*). *CA*, celiac artery

Materials and methods

Sonazoid (Daiichi Sankyo, Tokyo, Japan) is a solution containing lipid-stabilized MB filled with perfluorobutane gas. The average particle diameter is 2–3 μm, and the MB concentration is 1×10^9 MB/ml. We injected 0.12 μl MB/kg (0.015 ml/kg), the dose recommended specifically for clinical liver studies.[3]

Animals

Six 26- to 30-week-old WHHL rabbits (4 males, 2 females) weighing 3–4 kg were randomly selected. One 26-week-old male rabbit was the control. WHHL rabbits have been used for the evaluation of atherosclerotic lesions in a number of earlier studies.[2,6–10] All experiments were approved by our Animal Care and Use Committee and carried out according to the Guidelines for Animal Experimentation at our institution.

Ultrasonography studies

A clinical US system (Aplio XG; Toshiba Medical Systems, Tokyo, Japan) with a 12-MHz linear convex probe (PLT1202S; Toshiba Medical Systems) was used. The rabbits were deprived of food for 24 h before the experiments. They were anesthetized with an intramuscular injection of a mixture of ketamine hydrochloride 25 mg/kg (Ketalar 50; Sankyo Yell Yakuhin, Tokyo, Japan) and medetomidine hydrochloride 0.1 mg/kg (Domitor; Meiji Seika, Tokyo, Japan). Prior to MB infusion, the abdominal aorta was studied by fundamental B-mode imaging, and the celiac and superior mesenteric arteries were identified on sagittal views (Fig. 3a). The probe was then fixed in that position to observe the aortic wall.

Contrast enhancement was observed on harmonic B-mode pulse subtraction images. The frame rate was set at 10 frames/s (FPS) and the mechanical index at 0.2, as the pulse subtraction (PS)-low mode. After recording prestudy images in the PS-low mode, a bolus injection of MB was delivered via the auricular vein. US scanning was at 0.5, 2, 5, 10, and 20 min after MB delivery. An image acquired at 0.5 min after injection was the first-pass image of the IV-injected MB. Images obtained at other time points were used to monitor US signal changes. The aorta of a rabbit not injected with MB was the control.

Image analysis

During each observation period, US images were recorded digitally and analyzed offline with image processing software (Photoshop CS4 extended; Adobe Systems, San Jose, CA, USA). To evaluate contrast enhancement, a region of interest (ROI) was set at just below the boundary of the media adventitia and at the center of the aortic lumen (Fig. 1). The average image brightness of the ROI, defined as the videodensity,[4] of the aortic lumen and aortic wall was compared. We used 10×100 pixels and measured two data points in the aortic wall and lumen.

Histology for light microscopy and TEM

Abdominal aorta specimens from the WHHL rabbits were fixed in phosphate-buffered glutaraldehyde and paraformaldehyde and embedded in paraffin to obtain 5-μm serial transverse tissue sections. We used Mallory-Azan, elastica van Gieson (EVG), and hematoxylin and eosin (H&E) staining for general morphological analysis. For immunohistochemical staining we used a monoclonal antibody to RAM11 (1:500) (Dako, Glostrup, Denmark) as a primary antibody against macrophages.

A portion of the aorta and liver was embedded in gelatin, and 50 μm thick slices were cut on a vibratome (Microslicer DTK-3000W; Dosaka, Kyoto, Japan). The sections were dehydrated in a graded series of ethanol, embedded in aqueous acrylic resin (LR gold resin; London Resin, London, UK),[11–13] and polymerized in an ultraviolet cryo chamber (Pelco; Ted Pella, Redding, CA, USA) at −20°C. Thick polymerized sections were first examined to select the appropriate area for ultrastructural study under a phase-contrast light microscope (Diaphot TMD300; Nikon, Tokyo, Japan). Ultra-thin 70-nm sections were then prepared in an ultramicrotome

(Ultracut UCT; Leica, Vienna, Austria). Staining was with uranyl acetate and lead citrate for the TEM study (H-7500; Hitachi, Tokyo, Japan). Control specimens were obtained from one WHHL rabbit not injected with MB. An original solution of Sonazoid, prepared according to the above procedure, was used for the TEM study.

Statistical analysis

Differences in US signals from the vessel lumen and wall before and after MB injection were analyzed by analysis of variance (ANOVA) and Tukey's HSD correction. Differences between the vessel lumen and wall at each time point were analyzed with the *t*-test. $P < 0.05$ was considered significant. SPSS version 11.0 (SPSS, Chicago, IL, USA) was used for all analyses.

Results

US Images

The video-density in the aortic wall (intima–media complex, or IMC) acquired in PS-low mode was 8.48 ± 3.01 before MB injection and 10.96 ± 7.88, 32.42 ± 12.79, 24.55 ± 8.01, 17.73 ± 9.18, and 31.18 ± 13.35 at 0.5, 2, 5, 10, and 20 min, respectively, after MB injection. At the corresponding time points, the video-densities from the aortic lumen were, respectively, 1.16 ± 1.57, 64.21 ± 11.52, 53.59 ± 9.81, 13.32 ± 9.78, 2.63 ± 1.45, and 3.66 ± 3.01 (Fig. 2).

With the exception of the adventitia, under PS-low mode the US signals from the IMC and aortic lumen were almost undetectable prior to the injection of MB (Fig. 3b). At 0.5 min after injection, high echogenic MB was observed in the arterial lumen ($P < 0.05$) (Fig. 3c); and a linear, low-signal zone corresponding to the IMC was recognized. The video-density from the vessel lumen decreased after 5 min ($P < 0.05$), and a dot-like (or linear) high-echoic signal appeared at the IMC (Fig. 3d). The video-density of the IMC was significantly higher at 2 and 20 min after MB injection than before and 0.5 min afterward. There was no significant difference in the video-density of the IMC before and 5 or 10 min after injection. At 10 and 20 min after injection there was a significant difference between the video-density of the IMC and the lumen ($P < 0.05$).

Histology and immunohistochemistry

The aortic wall in all WHHL rabbits was clearly atherosclerotic. Large, raised intimal lesions with lipid cores were evident. They were acellular, comprised of lipid-rich debris including cholesterol clefts, and surrounded by a layer of foam cells. Many lipid-laden foam cells were also seen in the subendothelium (Fig. 4).

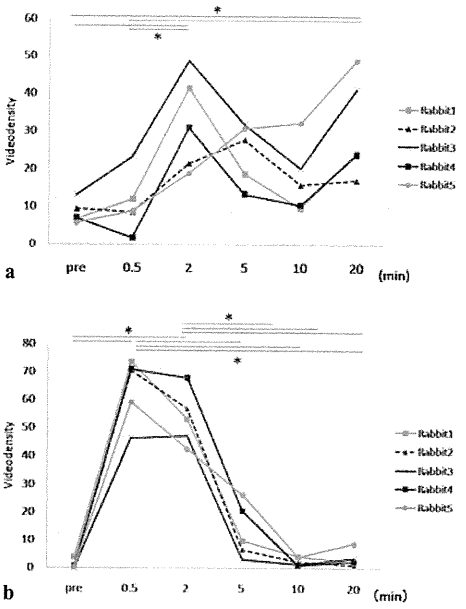

Fig. 2. Video-density of the aorta in rabbits. **a** Video-density of the aortic wall (intima–media complex, IMC). At 30 s after intravenous (IV) injection of the microbubble contrast agent (MB), the IMC appeared as a low-signal area. Before and 0.5 min after MB injection, the video-density of the IMC was almost the same. At 2 min after injection the video-density of the IMC peaked; it then decreased at 5–10 min after MB delivery. However, at 20 min after injection the video-density of the IMC was significantly higher than before and 0.5 min after injection. **b** Video-density of the aortic lumen. At 0.5–2.0 min after MB injection, the video-density of the aortic lumen showed a significant increase. At 5 min it began to decrease; the decline in video-density continued until it reached the preinjection level. $*P < 0.05$

The TEM revealed round 1- to 5-μm diameter particles distributed mainly in the lipid core[14] (Fig. 5a) that were similar to those present in the original solution (Fig. 5b). No MB was detected inside macrophages or in the capillary vessel lumen of the vasa vasorum.

Discussion

Atherosclerotic lesions in adult WHHL rabbits were evaluated using a US contrast agent. The US signal intensity (video-density) of the IMC was significantly higher at 20 min after MB injection than before or 0.5 min afterward. At 10 and 20 min after injection, the video-density of the IMC was significantly higher than that of the lumen. We attribute this to the contrast enhancement enabled by MB. At 10 or 20 min after

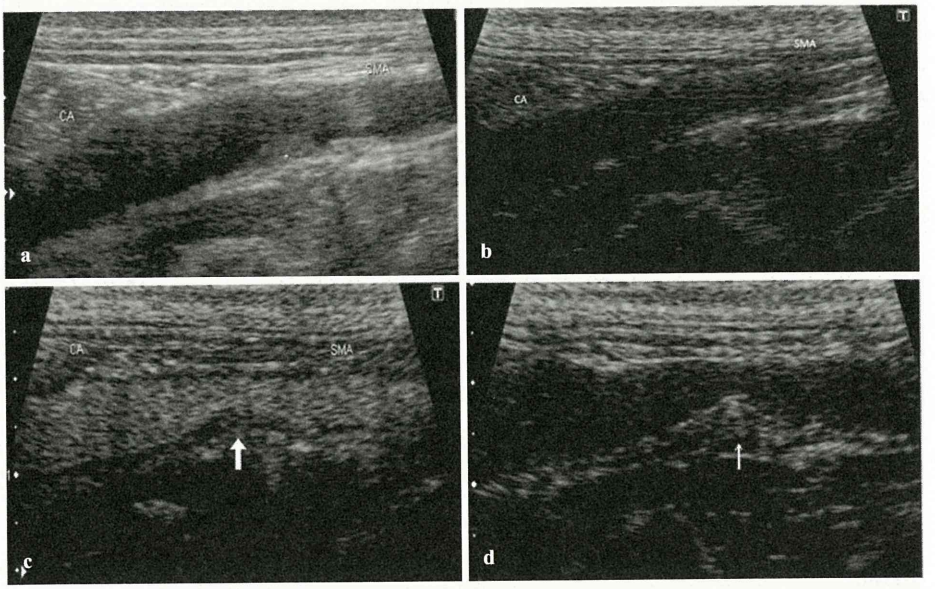

Fig. 3. Ultrasonography images. **a** Fundamental B-mode. **b** Before MB injection. It is difficult to identify the atherosclerotic lesions. **c** At 0.5 min after injection. High echogenic microbubbles are observed in the aortic lumen. **d** At 20 min after injection. Linear, high-echoic signals (*arrow*) appeared gradually on the surface of the IMC. **b–d** Harmonic B-mode pulse subtraction images. *CA*, celiac artery; *SMA*, superior mesenteric artery; *IMC*, intima–media complex

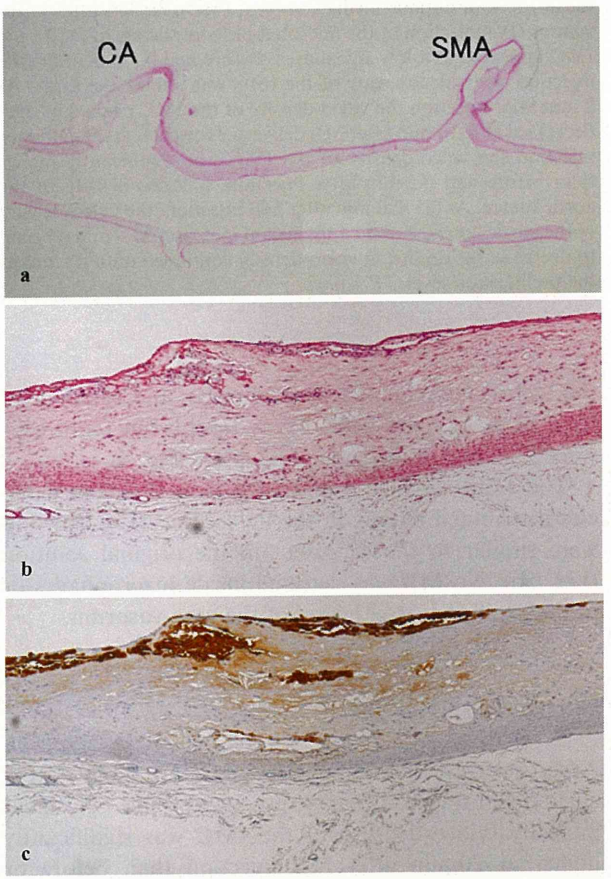

Fig. 4. Histological specimens of the rabbit abdominal aorta. **a** Loupe view. **b**, **c** ×40. **a**, **b** H&E stain. **c** Immunohistochemical stain (RAM11). The aortic wall shows evidence of atherosclerosis. Many RAM11-positive cells are seen in the plaque

injection there was little MB in the vessel lumen. We posit that contrast enhancement at these time points reflects the distribution of MB throughout the extravascular space. The video-density of the IMC was also significantly higher at 2 min after MB injection than before or 0.5 min afterward. The 2-min period corresponds to the vascular phase. We posit that our findings are indicative of the presence of MB in the capillary vessel lumen of the vasa vasorum because much MB persisted in the lumen at 2 min after injection.

We attribute the observed aortic wall enhancement to the presence of MB. TEM confirmed the presence of round structures, similar to those identified on TEM images of the original solution, in the extracellular matrix near the lipid core. Therefore, we considered the structures observed by TEM in the atherosclerotic plaques to be MB. All atherosclerotic lesions harbored abundant macrophages; they were always found in the subendothelium and around the plaque core. However, TEM identified no foam cells containing phagocytized MB. At 10 and 20 min after MB injection, the video-density of the lumen was lower than that of the IMC, suggesting that contrast-enhanced US imaging is useful for detecting vulnerable plaques. Ours is the first in vivo documentation of these phenomena in atherosclerotic lesions.

Sonazoid, an MB solution that is stable during US,[3,4] was developed to obtain consistent contrast enhancement on US images. Its properties are useful for early and delayed enhancement. Early enhancement reflects contrast-enhancing effects attributable to the intravascular presence of MB (the vascular phase). The agent

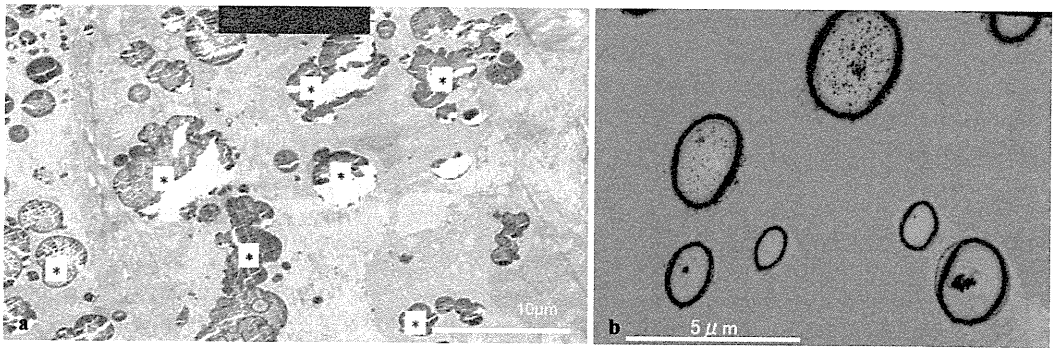

Fig. 5. Transmission electron microscopy study. **a** Note the round structures, thought to be MB, in the plaque core (*asterisks*). **b** Original Sonazoid solution. (**a** ×3000; **b** ×6000)

gradually disappears from the blood circulation and is incorporated into the reticuloendothelial system (RES). Furthermore, as the MB is phagocytosed by Kupffer cells, delayed (Kupffer) imaging is useful for detecting liver tumors in clinical US studies.[15–17]

We consider the round bodies shown in Fig. 5a to be MB because as in the original Sonazoid solution, the spheres were 2–3 μm in diameter, their surface was smooth, and their internal structure was uniform. Contrary to earlier reports,[18,19] our findings indicate that the 2- to 3-μm MB were able to migrate into atherosclerotic plaques.

The mechanisms underlying the migration of MB into vessels remain unclear. Although the intercellular gaps are wider between activated endothelial cells than in normal tissue, they are too narrow for the permeation by large particles such as Sonazoid.

The inner third of the aortic wall is fed by the blood flow and the outer two-thirds by the vasa vasorum from the adventitia side.[20] Although the normal vasa vasorum does not allow leakage, in the presence of atherosclerotic lesions it becomes permeable owing to the release of angiogenic factors such as vascular endothelial growth factor (VEGF). Because some newly generated vessels lack periocytes, various plasma components, including inflammatory cells, can leak out.[21] We used TEM to confirm that the identified structures were MB. As these structures were present in the extracellular matrix of the plaque core of MB-injected rabbits, we posit that MB leaked out of the vessels through the fragile vasa vasorum from the outside of the adventitia of the atherosclerotic artery.

Ultrasonography studies using MB contrast medium documented intraplaque neovascularization in carotid arteries.[21–24] Those studies assessed early enhancement to evaluate the degree of neovascularization as the level of angiogenesis represents a useful prognostic factor. By prolonging the observation time to include the delayed enhancement phase, we found that delayed contrast enhancement of the plaque recurred after the vascular phase, a phenomenon we attribute to vascular MB leakage. We consider our observations to be evidence of the fragility of the vessels. We also contend that our conclusion that MB is present in the capillary vessel lumen of the vasa vasorum and in the macrophages is not compromised by our observing only a small part of atherosclerotic lesions by TEM.

Various contrast agents used for the qualitative imaging of atherosclerotic lesions[25] reached the lesions and were extravasated by blood vessels. Nanoparticles such as ultra-small superparamagnetic iron oxide (USPIO)[10,26] and gadofluorine[9] have been used for magnetic resonance imaging, and N1177[27] has been used for CT studies. Others[28–30] reported using radioisotopes with a lower molecular weight, and some employed surface-modified MB with antibodies targeted at the endothelium.[31–33] The MB in those earlier reports remained attached only to the endothelial cell surface, and the presence of MB within the plaque core remained to be confirmed.

The clinical applicability of MB for purposes other than the detection of liver tumors varies.[16] The high echogenicity of Sonazoid administered IV may be useful for identifying vulnerable plaques. Our observations may lead to advances in the prognostic evaluation of atherosclerosis, and they may help in the assessment of the therapeutic effects of antilipidemic agents in patients with atheromatous plaques.[34]

Our study has some limitations. First, the optimal MB dose remains to be determined; the dose of Sonazoid we delivered was the one recommended for the diagnosis of human hepatic disease. Second, the detection sensitivity of US contrast enhancement was not sufficiently high for a precise diagnosis of the degree of atherosclerosis.

The most important diagnostic target is the coronary artery. To improve the quality of US images, further technological advances in image processing are necessary, as are better probes to detect echo signals from smaller targets.

Conclusion

In WHHL rabbits, prolonged contrast enhancement of the IMC was detected by US 10 and 20 min after MB injection.

Acknowledgments. We thank Mr. Takefumi Yamamoto (Central Research Laboratory, Shiga University of Medical Science) for technical assistance with the TEM. We also thank Mr. Yoshinori Saeki for excellent technical assistance with the histological specimens. This work was supported by a grant from the Japan Radiological Society in 2008 and received the silver medal at the annual meeting.

References

1. Van der Meer IM, Bots ML, Hofman A, del Sol AI, van der Kuip DA, Witteman JC. Predictive value of noninvasive measures of atherosclerosis for incident myocardial infarction: the Rotterdam Study. Circulation 2004;109:1089–94.
2. Shiomi M, Ito T, Yamada S, Kawashima S, Fan J. Correlation of vulnerable coronary plaques to sudden cardiac events: lessons from a myocardial infarction-prone animal model (the WHHLMI rabbit). J Atherosclerosis Thrombosis 2004;11: 184–9.
3. Watanabe R, Matsumura M, Chen CJ, Kaneda Y, Fujimaki M. Characterization of tumor imaging with microbubble-based ultrasound contrast agent, sonazoid, in rabbit liver. Biol Pharm Bull 2005;28:972–7.
4. Watanabe R, Matsumura M, Chen CJ, Kaneda Y, Ishihara M, Fujimaki M. Gray-scale liver enhancement with Sonazoid (NC100100), a novel ultrasound contrast agent; detection of hepatic tumors in a rabbit model. Biol Pharm Bull 2003;26:1272–7.
5. Moreno PR, Falk E, Palacios IF, Newell JB, Fuster V, Fallon JT. Macrophage infiltration in acute coronary syndromes: implications for plaque rupture. Circulation 1994;90:775–8.
6. Shindo J, Ishibashi T, Yokoyama K, Nakazato K, Ohwada T, Shiomi M, et al. Granulocyte-macrophage colony-stimulating factor prevents the progression of atherosclerosis via changes in the cellular and extracellular composition of atherosclerotic lesions in Watanabe heritable hyperlipidemic rabbits. Circulation 1999;99:2150–6.
7. Liang J, Liu E, Yu Y, Kitajima S, Koike T, Jin Y, et al. Macrophage metalloelastase accelerates the progression of atherosclerosis in transgenic rabbits. Circulation 2006;113: 1993–2001.
8. Shiomi M, Yamada S, Ito T. Atheroma stabilizing effects of simvastatin due to depression of macrophages or lipid accumulation in the atheromatous plaques of coronary plaque-prone WHHL rabbits. Atherosclerosis 2005;178:287–94.
9. Barkhausen J, Ebert W, Heyer C, Debatin JF, Weinmann HJ. Detection of atherosclerotic plaque with gadofluorine-enhanced magnetic resonance imaging. Circulation 2003;108: 605–9.
10. Kooi ME, Cappendijk VC, Cleutjens KB, Kessels AG, Kitslaar PJ, Borgers M, et al. Accumulation of ultrasmall superparamagnetic particles of iron oxide in human atherosclerotic plaques can be detected by in vivo magnetic resonance imaging. Circulation 2003;107:2453–8.
11. Fujimiya M, Okumiya K, Nakazawa M, Kitahama K, Kimura H, Maeda T. Effect of reserpine on 5-hydroxytryptophan (5HTP)-immunoreactive neurons in the rat brain. Histochemistry 1994;101:21–6.
12. Okumiya K, Matsubayashi K, Maeda T, Fujimiya M. Change in subcellular localization of gastrin-like immunoreactivity in epithelial cells of rat duodenum induced by carbachol. Peptides 1996;17:225–32.
13. Fujimiya M, Okumiya K, Kuwahara A. Immunoelectron microscopic study of the luminal release of serotonin from rat enterochromaffin cells induced by high intraluminal pressure. Histochem Cell Biol 1997;108:105–13.
14. Giuriato L, Scatena M, Chiavegato A, Zanellato AM, Guidolin D, Pauletto P, et al. Localization and smooth muscle cell composition of atherosclerotic lesions in Watanabe heritable hyperlipidemic rabbits. Arterioscler Thromb 1993;13:347–59.
15. Yanagisawa K, Moriyasu F, Miyahara T, Yuki M, Iijima H. Phagocytosis of ultrasound contrast agent microbubbles by Kupffer cells. Ultrasound Med Biol 2007;33:318–25.
16. Cosgrove D, Blomley M. Liver tumors: evaluation with contrast-enhanced ultrasound. Abdom Imaging 2004;29:446–54.
17. Hatanaka K, Kudo M, Minami Y, Ueda T, Tatsumi C, Kitai S, et al. Differential diagnosis of hepatic tumors: value of contrast-enhanced harmonic sonography using the newly developed contrast agent, Sonazoid. Intervirology 2008; 51(suppl 1):61–9.
18. Bartlett DW, Su H, Hildebrandt IJ, Weber WA, Davis ME. Impact of tumor-specific targeting on the biodistribution and efficacy of siRNA nanoparticles measured by multimodality in vivo imaging. Proc Natl Acad Sci U S A 2007;104:15549–54.
19. Greish K. Enhanced permeability and retention of macromolecular drugs in solid tumors: a royal gate for targeted anticancer nanomedicines. J Drug Targeting 2007;15:457–64.
20. Kumar V, Abbas AK, Fausto N, Mitchell RN. The blood vessels. In: Kumar V, Abbas AK, Fausto N, Mitchell RN, editors. Robbins basic pathology. 2007, pp 339–41. Philadelphia: Saunders Elsevier; 2007.
21. Feinstein SB. Contrast ultrasound imaging of the carotid artery vasa vasorum and atherosclerotic plaque neovascularization. J Am Coll Cardiol 2006;48:236–43.
22. Coli S, Magnoni M, Sangiorgi G, Marrocco-Trischitta MM, Melisurgo G, Mauriello A, et al. Contrast-enhanced ultrasound imaging of intraplaque neovascularization in carotid arteries: correlation with histology and plaque echogenicity. J Am Coll Cardiol 2008;52:223–30.
23. Vicenzini E, Giannoni MF, Puccinelli F, Ricciardi MC, Altieri M, Di Piero V, et al. Detection of carotid adventitial vasa vasorum and plaque vascularization with ultrasound cadence contrast pulse sequencing technique and echo-contrast agent. Stroke 2007;38:2841–3.
24. Shah F, Balan P, Weinberg M, Reddy V, Neems R, Feinstein M, et al. Contrast-enhanced ultrasound imaging of atherosclerotic carotid plaque neovascularization: a new surrogate marker of atherosclerosis? Vasc Med 2007;12:291–7.
25. Sanz J, Fayad ZA. Imaging of atherosclerotic cardiovascular disease. Nature 2008;451:953–7.
26. Ruehm SG, Corot C, Vogt P, Cristina H, Debatin JF. Ultrasmall superparamagnetic iron oxide-enhanced MR imaging of atherosclerotic plaque in hyperlipidemic rabbits. Acad Radiol 2002;9(suppl 1):S143–4.

27. Hyafil F, Cornily JC, Feig JE, Gordon R, Vucic E, Amirbekian V, et al. Noninvasive detection of macrophages using a nanoparticulate contrast agent for computed tomography. Nat Med 2007;13:636–41.
28. Ogawa M, Magata Y, Kato T, Hatano K, Ishino S, Mukai T, et al. Application of ^{18}F-FDG PET for monitoring the therapeutic effect of antiinflammatory drugs on stabilization of vulnerable atherosclerotic plaques. J Nucl Med 2006;47: 1845–50.
29. Rudd JH, Myers KS, Bansilal S, Machac J, Rafique A, Farkouh M, et al. (18)Fluorodeoxyglucose positron emission tomography imaging of atherosclerotic plaque inflammation is highly reproducible: implications for atherosclerosis therapy trials. J Am Coll Cardiol 2007;50:892–6.
30. Tawakol A, Migrino RQ, Bashian GG, Bedri S, Vermylen D, Cury RC, et al. In vivo ^{18}F-fluorodeoxyglucose positron emission tomography imaging provides a noninvasive measure of carotid plaque inflammation in patients. J Am Coll Cardiol 2006;48:1818–24.
31. Lindner JR, Song J, Christiansen J, Klibanov AL, Xu F, Ley K. Ultrasound assessment of inflammation and renal tissue injury with microbubbles targeted to P-selectin. Circulation 2001;104:2107–12.
32. Lindner JR, Song J, Xu F, Klibanov AL, Singbartl K, Ley K, et al. Noninvasive ultrasound imaging of inflammation using microbubbles targeted to activated leukocytes. Circulation 2000;102:2745–50.
33. Weller GE, Villanueva FS, Klibanov AL, Wagner WR. Modulating targeted adhesion of an ultrasound contrast agent to dysfunctional endothelium. Ann Biomed Eng 2002;30:1012–19.
34. Shiomi M, Ito T, Hirouchi Y, Enomoto M. Fibromuscular cap composition is important for the stability of established atherosclerotic plaques in mature WHHL rabbits treated with statins. Atherosclerosis 2001;157:75–84.

Differentiating atherosclerotic plaque burden in arterial tissues using femtosecond CARS-based multimodal nonlinear optical imaging

Leila B. Mostaço-Guidolin,[1] Michael G. Sowa,[1] Andrew Ridsdale,[2] Adrian F. Pegoraro,[2] Michael S. D. Smith,[1] Mark D. Hewko,[1] Elicia K. Kohlenberg,[1] Bernie Schattka,[1] Masashi Shiomi,[3] Albert Stolow,[2] and Alex C.-T. Ko[1,*]

[1]*Institute for Biodiagnostics, National Research Council Canada, Winnipeg, R3B 1Y6, Canada*
[2]*Steacie Institute for Molecular Sciences, National Research Council Canada, Ottawa, K1A 0R6, Canada*
[3]*Institute of Experimental Animals, Kobe University, School of Medicine, Kobe 650-0017, Japan*
**alex.ko@nrc-cnrc.gc.ca*

Abstract: A femtosecond CARS-based nonlinear optical microscope was used to simultaneously image extracellular structural proteins and lipid-rich structures within intact aortic tissue obtained from myocardial infarction-prone Watanabe heritable hyperlipidemic rabbits (WHHLMI). Clear differences in the NLO microscopic images were observed between healthy arterial tissue and regions dominated by atherosclerotic lesions. In the current ex-vivo study, we present a single parameter based on intensity changes derived from multi-channel NLO image to classify plaque burden within the vessel. Using this parameter we were able to differentiate between healthy regions of the vessel and regions with plaque, as well as distinguish plaques relative to the age of the WHHLMI rabbit.

OCIS codes: (170.3880) Medical and biological imaging; (170.4580) Optical diagnostics for medicine; (180.4315) Nonlinear microscopy; (300.6230) Spectroscopy, coherent anti-Stokes Raman scattering.

References and links

1. P. Libby, "Atherosclerosis: disease biology affecting the coronary vasculature," Am. J. Cardiol. **98**(12), S3–S9 (2006).
2. G. K. Hansson, "Inflammation, atherosclerosis, and coronary artery disease," N. Engl. J. Med. **352**(16), 1685–1695 (2005).
3. A. J. Lusis, "Atherosclerosis," Nature **407**(6801), 233–241 (2000).
4. B. K. Courtney, N. R. Munce, K. J. Anderson, A. S. Thind, G. Leung, P. E. Radau, F. S. Foster, I. A. Vitkin, R. S. Schwartz, A. J. Dick, G. A. Wright, and B. H. Strauss, "Innovations in imaging for chronic total occlusions: a glimpse into the future of angiography's blind-spot," Eur. Heart J. **29**(5), 583–593 (2008).
5. D. A. Bluemke, S. Achenbach, M. Budoff, T. C. Gerber, B. Gersh, L. D. Hillis, W. G. Hundley, W. J. Manning, B. F. Printz, M. Stuber, and P. K. Woodard, "Noninvasive coronary artery imaging: magnetic resonance angiography and multidetector computed tomography angiography: a scientific statement from the american heart association committee on cardiovascular imaging and intervention of the council on cardiovascular radiology and intervention, and the councils on clinical cardiology and cardiovascular disease in the young," Circulation **118**(5), 586–606 (2008).
6. Y. Honda, and P. J. Fitzgerald, "Frontiers in intravascular imaging technologies," Circulation **117**(15), 2024–2037 (2008).
7. P. G. Yock, and P. J. Fitzgerald, "Optimal Directional Coronary Atherectomy Final Results of the Optimal Atherectomy Restenosis Study (OARS)," Am. J. Cardiol. **81**, 27E–32E (1998).
8. J. M. Hodgson, K. G. Reddy, R. Suneja, R. N. Nair, E. J. Lesnefsky, and H. M. Sheehan, "Intracoronary ultrasound imaging: correlation of plaque morphology with angiography, clinical syndrome and procedural results in patients undergoing coronary angioplasty," J. Am. Coll. Cardiol. **21**(1), 35–44 (1993).
9. J. Sun, Z. Zhang, B. Lu, W. Yu, Y. Yang, Y. Zhou, Y. Wang, and Z. Fan, "Identification and quantification of coronary atherosclerotic plaques: a comparison of 64-MDCT and intravascular ultrasound," AJR Am. J. Roentgenol. **190**(3), 748–754 (2008).
10. P. Barlis, and J. M. Schmitt, "Current and future developments in intracoronary optical coherence tomography imaging," EuroIntervention **4**(4), 529–533 (2009).

#127944 - $15.00 USD Received 5 May 2010; revised 24 Jun 2010; accepted 25 Jun 2010; published 14 Jul 2010

11. P. Barlis, P. W. Serruys, A. Devries, and E. Regar, "Optical coherence tomography assessment of vulnerable plaque rupture: predilection for the plaque 'shoulder'," Eur. Heart J. **29**(16), 2023 (2008).
12. P. Barlis, G. Ferrante, F. Del Furia, and C. Di Mario, "In-vivo characterisation of coronary atherosclerosis with optical coherence tomography," Med. J. Aust. **188**(12), 728 (2008).
13. I. K. Jang, G. J. Tearney, B. MacNeill, M. Takano, F. Moselewski, N. Iftima, M. Shishkov, S. Houser, H. T. Aretz, E. F. Halpern, and B. E. Bouma, "In vivo characterization of coronary atherosclerotic plaque by use of optical coherence tomography," Circulation **111**(12), 1551–1555 (2005).
14. R. Rocha, L. Silveira, Jr., A. B. Villaverde, C. A. Pasqualucci, M. S. Costa, A. Brugnera, Jr., and M. T. T. Pacheco, "Use of near-infrared Raman spectroscopy for identification of atherosclerotic plaques in the carotid artery," Photomed. Laser Surg. **25**(6), 482–486 (2007).
15. Y. Komachi, H. Sato, and H. Tashiro, "Intravascular Raman spectroscopic catheter for molecular diagnosis of atherosclerotic coronary disease," Appl. Opt. **45**(30), 7938–7943 (2006).
16. J. T. Motz, M. Fitzmaurice, A. Miller, S. J. Gandhi, A. S. Haka, L. H. Galindo, R. R. Dasari, J. R. Kramer, and M. S. Feld, "In vivo Raman spectral pathology of human atherosclerosis and vulnerable plaque," J. Biomed. Opt. **11**(2), 021003 (2006).
17. G. V. Nogueira, L. Silveira, A. A. Martin, R. A. Zângaro, M. T. Pacheco, M. C. Chavantes, and C. A. Pasqualucci, "Raman spectroscopy study of atherosclerosis in human carotid artery," J. Biomed. Opt. **10**(3), 031117 (2005).
18. T. J. Römer, J. F. Brennan 3rd, G. J. Puppels, A. H. Zwinderman, S. G. van Duinen, A. van der Laarse, A. F. van der Steen, N. A. Bom, and A. V. Bruschke, "Intravascular ultrasound combined with Raman spectroscopy to localize and quantify cholesterol and calcium salts in atherosclerotic coronary arteries," Arterioscler. Thromb. Vasc. Biol. **20**(2), 478–483 (2000).
19. W. R. Zipfel, R. M. Williams, and W. W. Webb, "Nonlinear magic: multiphoton microscopy in the biosciences," Nat. Biotechnol. **21**(11), 1369–1377 (2003).
20. F. Helmchen, and W. Denk, "Deep tissue two-photon microscopy," Nat. Methods **2**(12), 932–940 (2005).
21. W. R. Zipfel, R. M. Williams, R. Christie, A. Y. Nikitin, B. T. Hyman, and W. W. Webb, "Live tissue intrinsic emission microscopy using multiphoton-excited native fluorescence and second harmonic generation," Proc. Natl. Acad. Sci. U.S.A. **100**(12), 7075–7080 (2003).
22. P. J. Campagnola, and L. M. Loew, "Second-harmonic imaging microscopy for visualizing biomolecular arrays in cells, tissues and organisms," Nat. Biotechnol. **21**(11), 1356–1360 (2003).
23. R. M. Williams, W. R. Zipfel, and W. W. Webb, "Interpreting second-harmonic generation images of collagen I fibrils," Biophys. J. **88**(2), 1377–1386 (2005).
24. A. Zoumi, A. Yeh, and B. J. Tromberg, "Imaging cells and extracellular matrix in vivo by using second-harmonic generation and two-photon excited fluorescence," Proc. Natl. Acad. Sci. U.S.A. **99**(17), 11014–11019 (2002).
25. J.-X. Cheng, and X. S. Xie, "Coherent Anti-Stokes Raman Scattering Microscopy: Instrumentation, Theory, and Applications," J. Phys. Chem. B **108**(3), 827–840 (2004).
26. C. L. Evans, E. O. Potma, M. Puoris'haag, D. Côté, C. P. Lin, and X. S. Xie, "Chemical imaging of tissue in vivo with video-rate coherent anti-Stokes Raman scattering microscopy," Proc. Natl. Acad. Sci. U.S.A. **102**(46), 16807–16812 (2005).
27. X. Nan, J.-X. Cheng, and X. S. Xie, "Vibrational imaging of lipid droplets in live fibroblast cells with coherent anti-Stokes Raman scattering microscopy," J. Lipid Res. **44**(11), 2202–2208 (2003).
28. Y.-M. Wu, H.-C. Chen, W.-T. Chang, J.-W. Jhan, H.-L. Lin, and I. Liau, "Quantitative assessment of hepatic fat of intact liver tissues with coherent anti-stokes Raman scattering microscopy," Anal. Chem. **81**(4), 1496–1504 (2009).
29. A. Zoumi, X. Lu, G. S. Kassab, and B. J. Tromberg, "Imaging coronary artery microstructure using second-harmonic and two-photon fluorescence microscopy," Biophys. J. **87**(4), 2778–2786 (2004).
30. M. B. Lilledahl, O. A. Haugen, C. de Lange Davies, and L. O. Svaasand, "Characterization of vulnerable plaques by multiphoton microscopy," J. Biomed. Opt. **12**(4), 044005 (2007).
31. H.-W. Wang, T. T. Le, and J.-X. Cheng, "Label-free imaging of arterial cells and extracellular matrix using a multimodal CARS microscope," Opt. Commun. **281**(7), 1813–1822 (2008).
32. T. T. Le, I. M. Langohr, M. J. Locker, M. Sturek, and J.-X. Cheng, "Label-free molecular imaging of atherosclerotic lesions using multimodal nonlinear optical microscopy," J. Biomed. Opt. **12**(5), 054007 (2007).
33. H.-W. Wang, I. M. Langohr, M. Sturek, and J.-X. Cheng, "Imaging and quantitative analysis of atherosclerotic lesions by CARS-based multimodal nonlinear optical microscopy," Arterioscler. Thromb. Vasc. Biol. **29**(9), 1342–1348 (2009).
34. A. F. Pegoraro, A. Ridsdale, D. J. Moffatt, Y. Jia, J. P. Pezacki, and A. Stolow, "Optimally chirped multimodal CARS microscopy based on a single Ti:sapphire oscillator," Opt. Express **17**(4), 2984–2996 (2009).
35. A. C.-T. Ko, A. Ridsdale, M. S. D. Smith, L. B. Mostaço-Guidolin, M. D. Hewko, A. F. Pegoraro, E. K. Kohlenberg, B. Schattka, M. Shiomi, A. Stolow, and M. G. Sowa, "Multimodal nonlinear optical imaging of atherosclerotic plaque development in myocardial infarction-prone rabbits," J. Biomed. Opt. **15**(2), 020501 (2010).
36. S. Tang, W. Jung, D. McCormick, T. Xie, J. Su, Y. C. Ahn, B. J. Tromberg, and Z. Chen, "Design and implementation of fiber-based multiphoton endoscopy with microelectromechanical systems scanning," J. Biomed. Opt. **14**(3), 034005 (2009).

#127944 - $15.00 USD Received 5 May 2010; revised 24 Jun 2010; accepted 25 Jun 2010; published 14 Jul 2010

37. G. Liu, T. Xie, I. V. Tomov, J. Su, L. Yu, J. Zhang, B. J. Tromberg, and Z. Chen, "Rotational multiphoton endoscopy with a 1 microm fiber laser system," Opt. Lett. **34**(15), 2249–2251 (2009).
38. M. Balu, G. Liu, Z. Chen, B. J. Tromberg, and E. O. Potma, "Fiber delivered probe for efficient CARS imaging of tissues," Opt. Express **18**(3), 2380–2388 (2010).
39. M. Shiomi, T. Ito, S. Yamada, S. Kawashima, and J. Fan, "Development of an animal model for spontaneous myocardial infarction (WHHLMI rabbit)," Arterioscler. Thromb. Vasc. Biol. **23**(7), 1239–1244 (2003).
40. M. Shiomi, T. Ito, S. Yamada, S. Kawashima, and J. Fan, "Correlation of vulnerable coronary plaques to sudden cardiac events. Lessons from a myocardial infarction-prone animal model (the WHHLMI rabbit)," J. Atheroscler. Thromb. **11**(4), 184–189 (2004).
41. P. Whittaker, R. A. Kloner, D. R. Boughner, and J. G. Pickering, "Quantitative assessment of myocardial collagen with picrosirius red staining and circularly polarized light," Basic Res. Cardiol. **89**(5), 397–410 (1994).
42. T. A. Pologruto, B. L. Sabatini, and K. Svoboda, "ScanImage: flexible software for operating laser scanning microscopes," Biomed. Eng. Online **2**(1), 13 (2003).
43. M. Strupler, A. M. Pena, M. Hernest, P. L. Tharaux, J. L. Martin, E. Beaurepaire, and M. C. Schanne-Klein, "Second harmonic imaging and scoring of collagen in fibrotic tissues," Opt. Express **15**(7), 4054–4065 (2007).
44. H. C. Stary, A. B. Chandler, R. E. Dinsmore, V. Fuster, S. Glagov, W. Insull, Jr., M. E. Rosenfeld, C. J. Schwartz, W. D. Wagner, and R. W. Wissler, "A definition of advanced types of atherosclerotic lesions and a histological classification of atherosclerosis. A report from the Committee on Vascular Lesions of the Council on Arteriosclerosis, American Heart Association," Circulation **92**(5), 1355–1374 (1995).
45. L. M. Buja, T. Kita, J. L. Goldstein, Y. Watanabe, and M. S. Brown, "Cellular pathology of progressive atherosclerosis in the WHHL rabbit. An animal model of familial hypercholesterolemia," Arteriosclerosis **3**(1), 87–101 (1983).
46. A. M. Seddon, N. Woolf, A. La Ville, R. M. Pittilo, P. M. Rowles, P. R. Turner, and B. Lewis, "Hereditary hyperlipidemia and atherosclerosis in the rabbit due to overproduction of lipoproteins. II. Preliminary report of arterial pathology," Arteriosclerosis **7**(2), 113–124 (1987).

1. Introduction

Atherosclerosis is a chronic progressive disease associated with plaque accumulation in the coronary, carotid and peripheral arteries [1–3]. Plaque development once considered to be a passive accumulation of lipids and cellular debris is now recognized as part of a complex process. Structurally, early disease manifests through a focal thickening of the endothelium and the formation of localized fatty streaks beneath the endothelium. Fatty streaks can progress to advanced lesions where lipid-laden cells and extracellular lipid droplets form a lipid rich necrotic core capped by vascular smooth muscle cells and a collagen-rich fibrous network [1,2]. Rupture or erosion of the fibrous cap results in the ejection of the lipid core into the vessel resulting in a clot or thrombosis that impedes blood flow in the artery. Imaging techniques are relied upon to detect blockages and localize plaques.

X-ray fluorescence angiography remains an important imaging modality for detecting and localizing stenotic lesions in patients [4]. However, 2D x-ray angiography cannot detect non-stenotic lesions making it of little value in quantifying plaque burden or as a tool for understanding plaque development. The ability of multi-detector computed tomography (MDCT) to detect calcified plaque is well established and preliminary studies suggest that MDCT may be able to distinguish between fat and fibrous as well as calcified tissue based on CT density values [5]. Coronary magnetic resonance imaging was also reported in classification and quantification of plaque burden, yet its relatively low resolution limits its clinical use [6]. Differentiation of plaque type and assessment of plaque burden, in-vivo, so far largely relies on the use of intravascular ultrasound (IVUS). Although IVUS allows visualization, in-vivo, of the geometry of the artery and atherosclerotic lesions [7–9], according to histopathological studies it suffers from low specificity and low sensitivity in detecting early lesions and lipid-rich lesions. Despite these short-comings IVUS has contributed significantly to our understanding of plaque development. Recently optical coherence tomography (OCT) and Raman spectroscopy were also reported to be useful in detecting and characterizing atherosclerotic lesions. Intravascular OCT shows particular promise and several research groups have demonstrated its potential [10–13] by characterizing plaque morphology at much higher resolution (~10 μm) than IVUS. Raman spectroscopy is ideal for identifying gross biochemical changes in tissue and has great potential to discriminate between lipid-rich, calcified and fibrotic plaques [14–18]. It is however a slower

#127944 - $15.00 USD Received 5 May 2010; revised 24 Jun 2010; accepted 25 Jun 2010; published 14 Jul 2010

technique limited by lower sensitivity. The recent trends in MDCT, IVUS and OCT to develop methods to differentiate tissue types underlines that both morphological and compositional information are crucial for understanding plaque development, plaque burden and predicting the risk of plaque rupture or erosion. Despite these advances in imaging, differentiation of types of plaque and assessment of plaque burden can only be verified by histological examination that conveys compositional information in a structural context.

As key structural protein constituents of the extracellular matrix, elastin and collagen are the dominant biomolecules associated with atherosclerotic disease progression. Similarly, modified cholesterols as the primary lipid species triggering plaque development are inextricably linked to the disease. Developing a practical method capable of interrogating these extracellular bio-molecules that are so closely linked to the disease is of great interest to many. Recently nonlinear optical (NLO) microscopic imaging has emerged as a powerful tool for label-free tissue imaging [19]. It is fast, biochemically specific and possess intrinsic 3-D resolution better than confocal microscopy. Two-photon excited fluorescence (TPEF), second-harmonic generation (SHG) and coherent anti-Stokes Raman scattering (CARS) have been intensively studied in imaging extracellular elastin, type-I collagen fibrils and lipid-rich molecules in bulk tissue without preparation or the use of dyes or stains [20–28]. Such label-free imaging capability renders NLO imaging well suited to understanding the role and interplay between these biochemical species in plaque development. In fact, TPEF and SHG have been used to study arterial tissue structures and atherosclerotic lesions previously [29–31]. First label-free NLO imaging of atherosclerotic lesions using three NLO modalities (TPEF, SHG and CARS) was reported recently by Le *et al* using a multimodal CARS microscope and an Ossabaw swine animal model of metabolic syndrome-induced arterial disease [32]. In this study they visualized CARS signals using two tightly synchronized pico-second laser beams and another femto-second Ti:sapphire laser for generating TPEF and SHG signals. Based on a similar optical setup and animal model, Wang *et al.* [33] also demonstrated quantitative measurements of collagen and lipids contents in atherosclerotic lesions on thin histological sections using a multimodal NLO microscope. Previously we have also demonstrated label-free atherosclerotic tissue imaging using a femtosecond CARS-based multimodal NLO microscope developed earlier [34] and myocardial infarction-prone Watanabe heritable hyperlipidemic (WHHLMI) rabbit strain [35]. The current study develops a quantitative metric based on the NLO images obtained from arterial tissue of WHHLMI rabbits and explores how this metric could be used to study the mechanisms of plaque development and quantify plaque burden. All measurements are performed on intact bulk tissue using backscattering detection (or Epi-) mode for its practicality for in vivo measurements. Endoscopic TPEF/SHG based on 2-D raster scanning and radial scanning were both reported in the literature [36,37]. Although endoscopic CARS has not been realized thus far due to challenges in dual laser-pulse delivery in the same optical fiber, progress in this direction was reported recently [38]. Thus, it is believed that with the fast advancement of new laser sources and nonlinear optical fiber, endoscopic multi-modal CARS could become a reality in the not too distant future. In this ex-vivo study we define an intensity based summary parameter from multimodal NLO images which correlates with atherosclerotic plaque burden in the WHHLMI rabbit model. This parameter also shows a marked dependence on the age of the animal. This dependence is consistent with the expected temporal pattern of plaque accumulation within the aorta of these rabbits.

Multimodal NLO imaging is capable of rapidly surveying bulk arterial tissue and can display information with respect to key biochemical components and structures that portend advanced atherosclerosis in the WHHLMI model. Along with this visual representation through TPEF, SHG and CARS images, simple intensity based parameters summarizing the images can be devised that correlate with disease burden and could be used to further quantify disease progression. Given the differences between human disease and the plaques developed by the WHHLMI model, this index is unlikely to be a good predictor of human plaque

#127944 - $15.00 USD Received 5 May 2010; revised 24 Jun 2010; accepted 25 Jun 2010; published 14 Jul 2010

pathology. However, the work demonstrates the possibility of developing similar indices predictive of human plaque composition and morphology from NLO imaging of human vessels.

2. Experimental

2.1. Animal model and tissue preparation

This study was approved by the local animal care committee at Institute for Biodiagnostics, National Research Council Canada. In this study, myocardial infarction prone Watanabe heritable hyperlipidemic rabbits, designated as WHHLMI rabbits [39,40], were used as an animal model to mimic spontaneous myocardial infarction in humans. Due to a hereditary defect in LDL processing, WHHLMI rabbits develop atherosclerotic plaques without requiring a modified diet. Four WHHLMI rabbits 4, 16, 17 and 24 months old, respectively, representing various stages of atherosclerotic disease progression were studied with the 24 months-old rabbit being considered to be nearing the end of its life cycle.

The three older rabbits used in the study were born and raised in the Institute for Experimental Animals, Kobe University, School of Medicine (Kobe, Japan) until they were at almost 12 months of age. These rabbits were later transported from Kobe University (Kobe, Japan) to the Institute for Biodiagnostics, National Research Council Canada (NRC-IBD). The younger rabbit used in the study was born at NRC-IBD.

The aorta was dissected from the ascending aorta to the external iliac artery and then rinsed in heparinized saline. The exterior aorta was delicately cleaned of connective tissue prior to being subdivided into ~20-30 mm sections resulting in 5-7 pieces. Additionally, some short segments were set aside for histology at this point. Each section was cut open longitudinally exposing the luminal surface. The samples were placed in petri-dishes with the luminal surface facing up on a moist surface and hydration was maintained throughout the measurements by periodically applying phosphate buffered saline (PBS) solution to the tissue. Digital photos of the luminal surface were acquired and regions of interest were identified prior to measurements.

For histology, the artery was cross-sectioned on a cryotome into sections 8μm in thickness while embedded in OCT (optical cutting temperature) cutting medium. Adjacent artery sections were used in multimodal CARS imaging, H&E (hematoxylin and eosin) staining to reveal general tissue morphology, picro-sirius red staining for highlighting collagen, and oil red O staining for accenting lipid content. The tissue sections prepared for CARS imaging received no further treatment after cutting while those prepared for histology were immersion-fixed in either 95% ethanol or 10% buffered formalin based on individual staining protocols. In visualizing collagen, cross-handed circularly-polarized microscopy was employed to provide higher contrast [41]. Histology images were obtained using a 10x air objective lens on a Zeiss Axio Observer Z1 system equipped with AxioCam ICc3 CCD camera (Carl Zeiss Canada, Toronto, ON, Canada).

2.2. Femtosecond CARS-based multimodal NLO microscopic imaging

A home-built multimodal nonlinear optical (NLO) laser scanning microscope illustrated in Fig. 1 was used for TPEF, SHG and CARS imaging of arterial tissues and was described previously [35]. The light source for TPEF and SHG imaging was a Ti:Sapphire oscillator (Tsunami, Spectra-Physics) centered at 800 nm with a 100 fs pulse duration and a 20 nm bandwidth. Average output power was measured at 1W when the oscillator was pumped with a 7.25 W green laser at 532 nm (Millennium Pro, Spectra-Physics). A Faraday isolator (Newport) was placed close to the emission exit of the Ti:Sapphire oscillator to prevent any back reflections of the femto-second pulses from re-entering the laser cavity. Re-compression of the pulses was accomplished using a pair of GTI laser mirrors (Layertec GmbH, Germany)

#127944 - $15.00 USD Received 5 May 2010; revised 24 Jun 2010; accepted 25 Jun 2010; published 14 Jul 2010

in compensation for the large positive group velocity dispersion (GVD) introduced by Faraday isolator and other microscope optics.

The femto-second pulse was then split into two beams using a 50:50 beam splitter. The reflected pulses were used as the pump beam for CARS imaging and also as the light source for TPEF and SHG imaging. Approximately 300mW transmitted pulse after the beam splitter was coupled into a PCF (NL-1.4.775-945, NKT Photonics A/S, Denmark) through a 20x objective lens (Newport) generating a broadband emission both in the visible and in the near infrared (NIR). The NIR portion (>900nm) of this broadband emission was used as the Stokes beam for CARS imaging. The pump and Stokes pulses were combined at a beam combiner before proceeding into the laser scanning microscope assembly. A 20x, 0.75 NA infinity corrected air objective lens (Olympus Canada, Markham, ON, Canada) focused the laser pulses on samples and also collected the epi-TPEF/SHG/CARS signals. The collected NLO signals were transmitted to three non-descanned PMT detectors (H9656 series, Hamamatsu, Bridgewater, NJ, USA) mounted on the microscope assembly for simultaneous TPEF, SHG and CARS imaging at 530 ± 20nm, 400 ± 30nm and 630 ± 30nm, respectively. Typically 25mW of pump and 8mW of Stokes (measured after the 20x air objective lens) were used for imaging.

ScanImage (ver. 3.5) software [42] was used for image acquisition and laser scanning control. Pixel dwell time for an average of 4 scans for a single collection was 21 μs. Post image viewing and 3 channels separation were performed in ImageJ ver 1.42b. Image background correction, intensity normalization and calculation of various image parameters were carried out using Matlab.

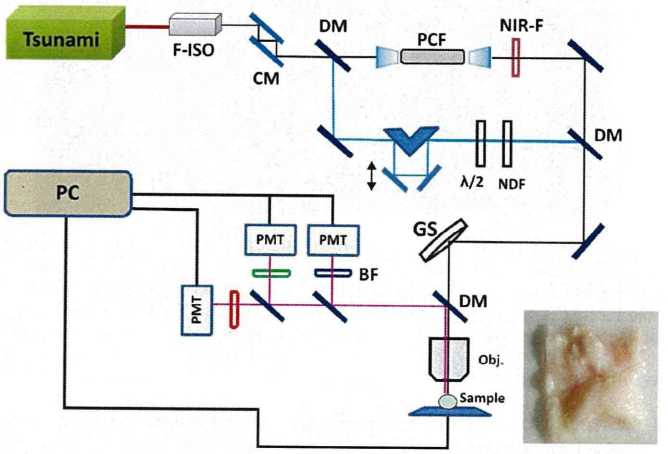

Fig. 1. Schematic of the home-built multimodal nonlinear optical laser scanning microscope. Light source for TPEF and SHG imaging is a Ti:Sapphire femto-second oscillator (Tsunami,Spectra-Physics). For CARS imaging, Stokes pulses are generated in PCF which is pumped by the same Ti:sapphire laser. Inset shows a typical video image of a tissue sample with lumen surface facing up. F-ISO: Faraday isolator; CM: chirp laser mirrors; BS: beam splitter; NIR-F: near-IR filter;; GS: galvo scanner; DM: dichroic mirror; OBJ: objective lens; BF: bandpass filter; NDF: neutral density filter; λ/2: half waveplate.

3. Results and discussion

3.1. Validating multimodal CARS imaging with histology

Three different types of histological stains were compared with the multimodal CARS image of an adjacent unstained artery section in Fig. 2. Figure 2A, 2B and 2C illustrate H&E (bright field), picro-sirius red (circularly polarized light) and oil red O (bright field) stains of adjacent artery sections, respectively, to help visualize general tissue morphology and particular extra-

#127944 - $15.00 USD Received 5 May 2010; revised 24 Jun 2010; accepted 25 Jun 2010; published 14 Jul 2010

cellular components. Three major biochemical components relevant to atherosclerotic plaque development, extra-cellular elastin in tunica media, collagen fibrils in tunica adventitia, on intima-media boundary and forming the cap on the atherosclerotic plaque as well as lipids in plaque bodies are all correctly visualized in a multimodal CARS image with elastin fiber color-coded in green (TPEF), collagen fibrils in blue (SHG) and lipids in red (CARS) (shown in Fig. 2D). The correspondence between the histological sections and the multimodal CARS images validates our understanding of what gives rise to contrast in the multimodal CARS image. This validation ensures accurate interpretation of multimodal CARS imaging in presenting the biochemical composition of atherosclerotic lesions.

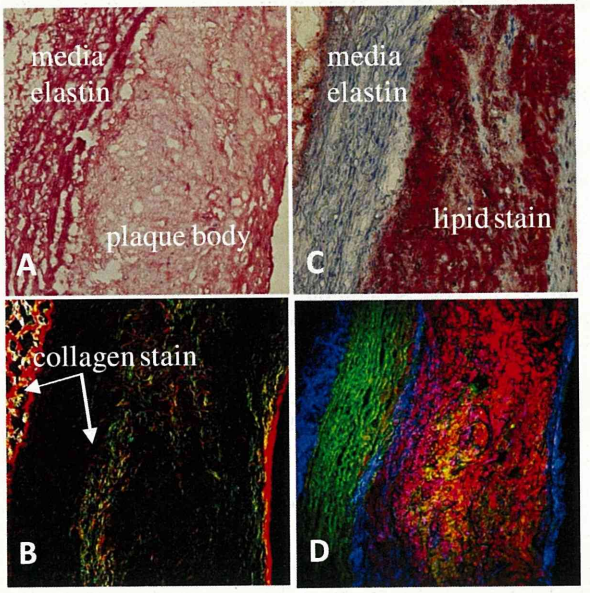

Fig. 2. Comparison of (A) H&E (B) picro-sirius red (C) oil red O histological stain with (D) label-free multimodal CARS image of adjacent artery cross-sections. Color-codes shown in (D): green is TPEF representing mainly elastin, blue is SHG representing mainly collagen fibrils and red is CARS representing mainly lipids content. Both SHG and CARS signals are collected in the forward-direction while TPEF is collected in the backscattered (epi-) direction.

3.2. Scoring and image evaluation

Collagen fibril scoring was previously developed using parameters extracted from collagen SHG images, according to Strupler *et. al.* [43]. In that work the authors used three phenomenological scores, D, S, and SF to quantify the distribution and morphology of collagen fibrils in unlabeled fibrotic murine kidney tissue sections using SHG images, where D (density) is the volume density of pixels exhibiting a significant SHG signal; S (signal) is the average value of the SHG signal in a corrected SHG image and SF (signal in fibers) is the ratio of the other two scores: SF = S/D representing average SHG signal intensity in regions exhibiting significant SHG signals.

This method worked well in scoring collagen in sectioned kidney tissue but may prove challenging in classifying complex biological structures such as atherosclerotic lesions using multi-dimensional information (SHG for collagen, TPEF for elastin and other fluorescent particles and CARS for lipid-rich structure) derived from a bulk tissue due to pathological interplay of extracellular components in an atherosclerotic lesion. In order to address the complexity and the dynamic nature of atherosclerotic disease progression, we developed a new parameter that can accurately track plaque burden in the vessel using biochemical data collected through combined elastin, collagen and lipid imaging.

#127944 - $15.00 USD Received 5 May 2010; revised 24 Jun 2010; accepted 25 Jun 2010; published 14 Jul 2010

Following the approach proposed by Strupler *et al* for analyzing fiber score in SHG images, three SF scores were extracted from individual SHG, CARS and TPEF, but co-registered, images of the same sample. Parameters D and S were calculated for all TPEF, SHG and CARS images using definitions given by Stupler *et al.* [43]. Note that Strupler *et al* define S/D as a signal in fibres score (SF), but in this study we are using a more generic term, called significant signal score (SS), since not all three imaging channels (SHG, CARS and TPEF), represent biomolecules that have fibrous structures. A significant signal score (SS) was calculated for each image using the equation SS = S/D.

Each individual image (SHG, CARS or TPEF) was first corrected for PMT dark signals and for the PMT amplification level used in different channels by normalizing the whole image to a pre-determined PMT amplification curve. Three SS scores (SS_{SHG}, SS_{CARS} and SS_{TPEF}) were calculated using the corrected SHG, CARS and TPEF images collected over the same sampling location.

3.3. Significant signal score (SS) – correlation with rabbits' age

In order to calculate the significant signal score (SS), multimodal epi-NLO images were acquired from smooth/healthy luminal surface and atherosclerotic plaques of four WHHLMI rabbits of different ages, 4, 16, 18, and 24 months-old, respectively.

In Fig. 3 some examples of how those regions looks under our multimodal NLO microscope. Figure 3A was acquired at a healthy region of the arterial lumen of a 4 months-old rabbit, while Figs. 3C, 3E and 3G were acquired from healthy lumen of the 16, 18, and 24 months-old rabbits, respectively. The images in Fig. 3B, 3D, 3F, and 3H were acquired from atherosclerotic plaques found in rabbits of 16, 18, and 24 months-old, respectively. The co-localized TPEF/CARS/SHG images acquired by three separate detection channels of the microscope are represented by different colors where TPEF signal is presented in green, CARS signal is presented in red and SHG signal is presented in blue.

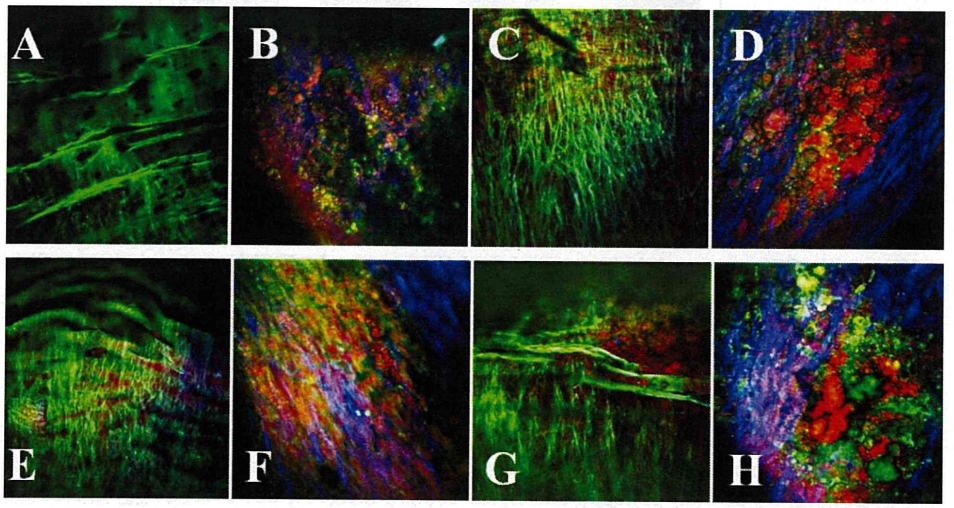

Fig. 3. Representative multimodal epi-NLO image acquired from smooth/healthy luminal surface of the WHHLMI rabbit artery, that is (A) 4 months-old, (C) 16 months-old, (E) 18 months-old, (G) 24 months-old, and atherosclerotic plaques found on the WHHLMI rabbit arteries at (B) 4 months-old, (D) 16 months-old, (F) 18 months-old, and (H) 24 months-old. (20x air objective lens, 0.75 NA).

In a representative NLO image of a healthy lumen, Fig. 3A, only the luminal elastic lamina is clearly visible from the TPEF signal and neither lipid-rich structures nor collagen fibrils in the CARS and SHG signals are evident. On the contrary, Fig. 3H, a representative

#127944 - $15.00 USD Received 5 May 2010; revised 24 Jun 2010; accepted 25 Jun 2010; published 14 Jul 2010

NLO image from the surface of an advanced arterial plaque, shows abundant lipid-rich structures (CARS in red), collagen fibrils (SHG in blue) along with strongly fluorescent (TPEF in green) macromolecules differing in structure from the luminal elastic lamina that dominate the images of healthy vessels illustrated in Fig. 3A. The enhanced SHG intensity arising from collagen fibrils and the CARS intensity arising from lipid-rich structures, from regions of plaque (see Fig. 3B, 3D, 3F and 3H) are consistent with known plaque pathology and explain the increased SS_{SHG} and SS_{CARS} scores from regions of plaque; however, the SS_{TPEF} score shows no obvious difference between regions of plaque and healthy vessel. The diminishing elastin content at the region of plaque is compensated for by an increasing number of other fluorescent macromolecules detected by TPEF.

In order to better illustrate the change in SS scores with respect to plaque progression represented by the age of the rabbit, the mean SS scores obtained from the images of four rabbits (4, 16, 18, and 24 months-old) are presented in Fig. 4.

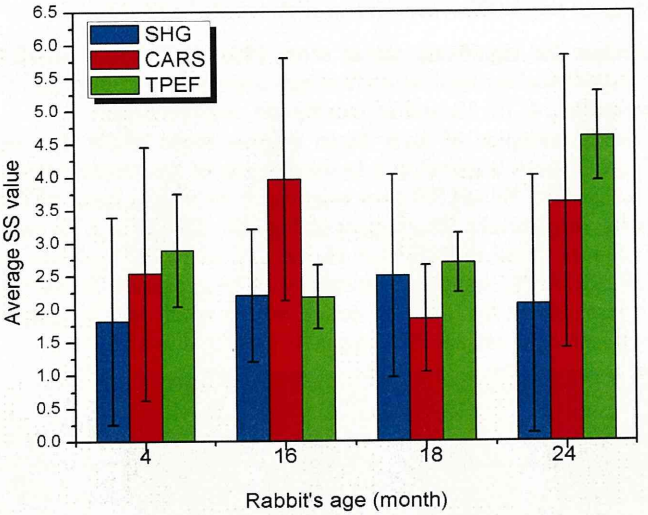

Fig. 4. Comparison of the SS scores extracted from SHG, CARS and TPEF images acquired from the arterial lumen of four WHHLMI rabbits: 4 months-old, 16 months-old, 18 months-old and 24 months-old.

The mean SS scores and their standard deviations were obtained by averaging over all SS scores extracted from all of the measurement locations including healthy and atherosclerotic luminal surfaces, along the same artery of the same animal. A total of 31, 29, 38 and 40 different locations were measured for the 4 months-old, 16 months-old, 18 months-old, and 24 months-old rabbit, respectively, resulting in approximately 800 processed images.

According to the data presented in Fig. 4, it is clear that it is not possible to differentiate atherosclerotic plaque burden using any of the SS scores as there is no evident correlation. In principle when atherosclerotic plaques become worse, it should lead to an increase of SHG and CARS signals as both collagen and lipids content increase; however, SS_{SHG} and SS_{CARS} scores are not increasing proportional to plaque development: the SS_{SHG} score for the youngest rabbit (4 months-old) is 1.8 ± 2.6 and for the oldest one (24 months-old) it is 2.1 ± 3.0 Considering the spread of the scores as evident from the standard deviations of both values, it can be concluded that these values are not statistically significant different, therefore SS scores alone is not a good parameter to use to differentiate plaque burden.

#127944 - $15.00 USD Received 5 May 2010; revised 24 Jun 2010; accepted 25 Jun 2010; published 14 Jul 2010

3.4. Optical index for plaque burden (OIPB)

As discussed in previous sections, the mean SS scores generally are well correlated in scoring collagen in sectioned kidney tissue, but they are not reliable indicators for distinguishing atherosclerotic plaques. For instance, some NLO images taken from advanced plaques are abundant in lipid-rich structures but show no collagen fibrils (e.g. lipid-rich type-IV atheroma). Others show a high density of collagen fibrils along with abundant lipid (e.g. collagenous type-V_a fibrous atheroma). Although both lesion types are considered advanced, the lower SS_{SHG} score derived from a type IV atheroma might underestimate disease severity. We propose a new optical index for plaque burden, or OIPB index.

Considering the images presented in Fig. 5, which are organized based on the level of plaque burden, it is possible for us to define some patterns of changes in all three NLO signal channels. Figure 5A–5C show examples of healthy arterial lumen; Fig. 5D shows an atherosclerotic lesion found in a young rabbit artery; Fig. 5E is an atherosclerotic plaque, where it is possible to note some collagen fibers formation (shown blue); Fig. 5F is an atherosclerotic plaque with higher lipid (shown red) content; Fig. 5G is an atherosclerotic plaque containing a high density of collagen fibers and lipids, and finally Fig. 5H is a very advanced plaque.

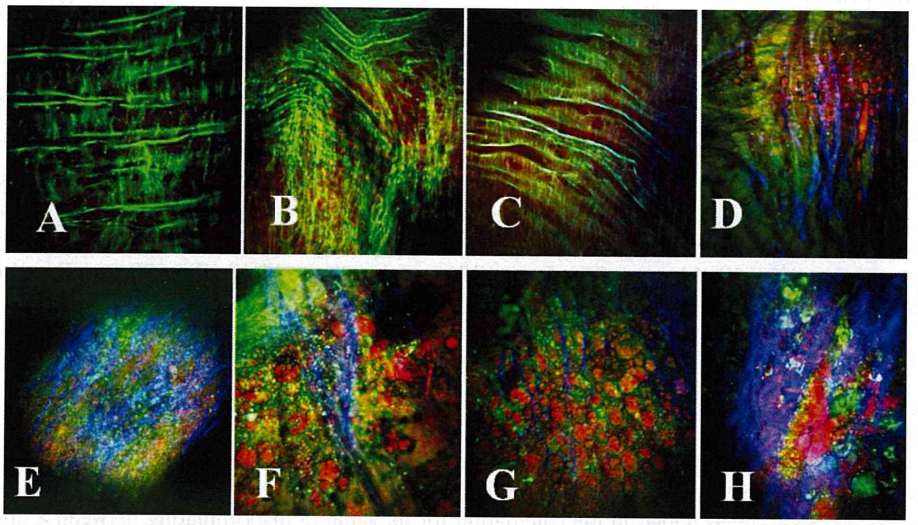

Fig. 5. Representative multimodal epi-NLO image acquired from the luminal surface of WHHLMI rabbit arteries, with (A) -(C) healthy lumen; (D) early atherosclerotic plaque found in young rabbit; (E) atherosclerotic plaque (with dense collagen fibers shown blue); (F) atherosclerotic plaque with higher lipid content shown red; (G) atherosclerotic plaque containing collagen fibers and lipids, and (H) very advanced plaque (20x air objective lens, 0.75 NA).

The three average SS values for each image shown in Fig. 5 are calculated and then presented in Fig. 6 where the SS_{SHG} and SS_{CARS} scores are associated with collagen and lipids (both are associated with plaque regions), respectively, and SS_{TPEF} scores can be associated with elastin in healthy tissue or with other fluorescent macromolecules in the region of plaque.

#127944 - $15.00 USD Received 5 May 2010; revised 24 Jun 2010; accepted 25 Jun 2010; published 14 Jul 2010

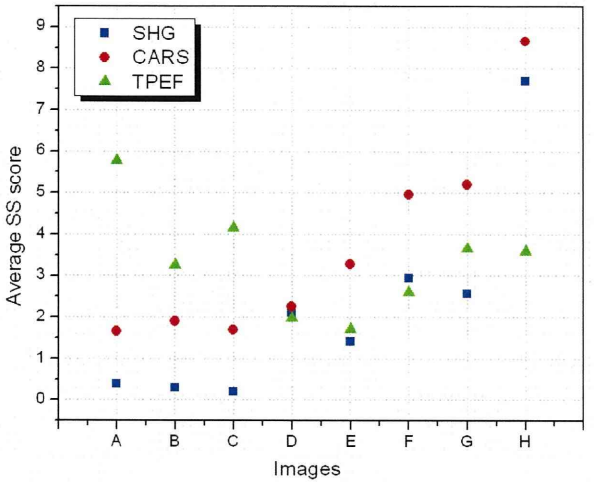

Fig. 6. Average SS scores extracted from SHG (blue squares), CARS (red circles) and TPEF (green triangles) images acquired from the arterial lumen of WHHLMI rabbits. Images A-H correspond to those shown in Fig. 5

From Fig. 6, we clearly observe a pattern for each of the SS scores, which can be summarized as follows. The healthier the tissue is, the lower the SS_{SHG} and the SS_{CARS} but the higher the SS_{TPEF}. The opposite is true if the tissue has an increased burden of plaque. In addition, we can also observe a correlation between the differences between the three SS scores based on the health of the tissue. For instance, the healthier the tissue is, as the greater the difference between SS_{SHG} and SS_{TPEF}, with SS_{TPEF} being higher than SS_{SHG}; and also the greater the difference between SS_{CARS} and SS_{TPEF}, with SS_{TPEF} higher than SS_{CARS}. Based on these observations, an OIPB index can be defined by the equation,

$$OIPB = SS_{SHG} + SS_{CARS} + d\left(SS_{SHG}, SS_{TPEF}\right) + d\left(SS_{CARS}, SS_{TPEF}\right) + d\left(SS_{CARS}, SS_{SHG}\right) \quad (1)$$

where the terms $d(SS_X, SS_Y)$ are the difference between two SS scores (SHG, CARS and TPEF), $d(SS_x, SS_y) = SS_x - SS_y$. Note that SS_{TPEF} score alone was not included in the calculation of OIPB indices because it provides no additional contrast in discriminating between atherosclerosis lesions from healthy vessel wall as mentioned earlier. A term $d(SS_{CARS}, SS_{SHG})$ was added in the calculation for its value in discriminating between a lipid-rich type-IV atheroma and a type-V fibrous atheroma. OIPB indices were calculated for all NLO images and were normalized using the same method described earlier.

3.5. OIPB index of the arterial lumen as a function of plaque burden

In order to better illustrate the utility of the OIPB index Fig. 7 plots the mean OIPB index obtained from images of the lumen surface from healthy ($OIPB_{healthy}$) and atherosclerotic ($OIPB_{athero}$) regions for each rabbit presented in the order of the age of the rabbit. In all cases, $OIPB_{athero}$ is significantly higher than $OIPB_{healthy}$. The OIPB index from regions of plaque increase in a linear fashion with the age of the WHHLMI rabbit, representing the overall burden of plaque in the aorta.

#127944 - $15.00 USD Received 5 May 2010; revised 24 Jun 2010; accepted 25 Jun 2010; published 14 Jul 2010